Applied Mathematical Modelling 36 (2012) 4003–4019

Contents lists available at SciVerse ScienceDirect

Applied Mathematical Modelling

journal homepage: www.elsevier.com/locate/apm

On an inverse problem: Recovery of non-smooth solutions to backward heat equation

Fabien Ternat [a], Prabir Daripa [a,*], Oscar Orellana [b]

[a] Department of Mathematics, Texas A&M University, College Station, TX, United States
[b] Departamento de Matemáticas, Universidad Técnica Santa María de Valparaíso, UTFSM, Chile

ARTICLE INFO

Article history:
Received 13 October 2010
Received in revised form 1 October 2011
Accepted 2 November 2011
Available online 11 November 2011

Keywords:
Heat equation
Inverse problem
Illposed problem
Finite difference methods
Quasi-reversibility techniques
Non-smooth solutions

ABSTRACT

We have recently developed two quasi-reversibility techniques in combination with Euler and Crank–Nicolson schemes and applied successfully to solve for smooth solutions of backward heat equation. In this paper, we test the viability of using these techniques to recover non-smooth solutions of backward heat equation. In particular, we numerically integrate the backward heat equation with smooth initial data up to a time of singularity (corners and discontinuities) formation. Using three examples, it is shown that the numerical solutions are very good smooth approximations to these singular exact solutions. The errors are shown using pseudo-*L*- and *U*-curves and compared where available with existing works. The limitations of these methods in terms of time of simulation and accuracy with emphasis on the precise set of numerical parameters suitable for producing smooth approximations are discussed. This paper also provides an opportunity to gain some insight into developing more sophisticated filtering techniques that can produce the fine-scale features (singularities) of the final solutions. Techniques are general and can be applied to many problems of scientific and technological interests.

1. Introduction

Recovering non-smooth solutions of an illposed problem is a highly non-trivial task. Nonetheless, such problems arise in many applications of practical interest and many such problems are parabolic in nature. For example, such problems arise in many applied areas such as in contaminant transport, in medical imaging, in geophysics and exploration and so on. There are many such problems that arise also in modeling of fluid flows in a variety of applications such as vortex dynamics, water waves, free or moving boundary problems and so on (see [1–4]). Due to short wave instability that are associated with these kinds of illposed problems, development of robust numerical methods is still an unsolved problem in computational science. There is not a single numerical method known-to-date that can be used (without any *a priori* knowledge of the singularity in the associated PDE) in an algorithmic fashion to find the nature of singularity and its time of formation numerically. It is almost always that such problems have been dealt numerically in combination with some theoretical knowledge that facilitates choice of numerical parameters to recover what one has prior knowledge of (see [5,6]). The development of robust methods is needed so that numerically these issues of time of and nature of singularity formations for illposed problems suffering from short waves can be addressed numerically. For making progress in this direction, it is necessary first to carefully develop numerical methods for linear illposed problems before attacking nonlinear problems of the kind arising

* Corresponding author.
E-mail address: prabir.daripa@math.tamu.edu (P. Daripa).

0307-904X/$ - see front matter © 2011 Elsevier Inc. All rights reserved.
doi:10.1016/j.apm.2011.11.020

in fluid mechanics and other applied areas. Numerical experiments with linear problems can be rewarding in gaining insight and developing robust methods. This has been the primary motivation for this paper.

In this paper we take such a prototype linear illposed problem, namely recovering smooth approximations of non-smooth solutions of a backward heat equation subject to smooth initial data. We apply our recently developed two quasi-reversibility techniques (see [7]) in combination with Euler and Crank–Nicolson schemes. Numerical results as well as errors using pseudo-*L*- and *U*-curves are presented and analyzed.

The problem of heat conduction through a conducting medium occupying a unit space $[0,1]$ subject to no heat flux across the boundary of the region is formulated as follows.

$$\begin{cases} u_t - \nu u_{xx} = 0, \quad x \in [0,1], \quad t > 0, \\ u_x|_{\partial\Omega} = 0, \quad t > 0, \\ u(x,0) = u_0(x), \quad x \in [0,1]. \end{cases} \tag{1}$$

Here $u(x,t)$ is the temperature and $u_0(x)$ is the initial temperature distribution. This problem is known to be well-posed in the sense of Hadamard, i.e. existence, uniqueness and continuous dependence of the solution on the boundary data are well-established for this problem. The above problem is usually referred as a forward problem in the context of heat equation.

The corresponding backward problem is the problem of finding the initial temperature distribution of the forward problem from a knowledge of the final temperature distribution $v_0(x)$ at time T_0.

$$\begin{cases} u_t - \nu u_{xx} = 0, \quad x \in \Omega, \quad t \in [0,T], \\ u_x|_{\partial\Omega} = 0, \\ u(x,T) = v_0(x), \quad x \in [0,1]. \end{cases} \tag{2}$$

It is convenient to rewrite this problem, by the change of variable $t \to T_0 - t$, in terms of backward variable $v(x,t) = u(x,T_0 - t)$:

$$\begin{cases} v_t + \nu v_{xx} = 0, \quad x \in \Omega, \quad t \in [0,T_0], \\ v_x|_{\partial\Omega} = 0, \\ v(x,0) = v_0(x), \quad x \in [0,1]. \end{cases} \tag{3}$$

It is well known that there is a lack of existence, uniqueness and continuous dependence of solutions of this backward problem on any arbitrary initial data (see [8–11]). Although, for some specific initial data, this problem can be well-posed [10] in theory, existence of such data is rare in practice due to the presence of noise in the data for various reasons including error in the measured data. Numerical integration of such equations by any numerical scheme further compounds this problem due to the effect of truncation and round-off errors. (see [12,13,9,14]).

A constructive approach to circumvent this computational challenge is to analyze first the dispersion relation. The dispersion relation associated with the backward heat equation is $\omega = k^2$, i.e. a mode with wave number k grows quadratically. This kind of catastrophic growth of short waves is also an indication that (classical) solutions of the backward problem may not always exist for all time for arbitrary initial data. This is all too well known for the backward heat equation because we know that any discontinuous temperature profile gets smoothed out instantaneously by forward heat equation. Another consequence of this is the undesirable catastrophic growth of errors (in particular in high wave number modes) arising due to numerical approximation of the equation (truncation error), the machine representation of the data (roundoff error) and noise in any measured data.

In a recent paper (see [7]), we presented results of our numerical study on the backward heat equation with initial data which were finite time solutions of the forward problem with smooth initial data. Purpose in [7] was to (i) propose two schemes for solving this equation in conjunction with regularization techniques including filtering (see [5,15,12,16,17]) and structural perturbation of the heat equation; and (ii) then to test their suitability for stable computations by proper choice of numerical and regularization parameters. There we have shown suitability of these methods and their limitations by showing various error plots. In this paper, we continue similar study but with initial data which are final solutions of the forward heat equation starting with *non-smooth* data. The goal here is to test whether these numerical methods are also suitable for computing smooth solutions which are good approximations to the exact non-smooth solutions. The numerical results including error plots suggest that these methods when applied properly are suitable for this purpose.

In closing this section, it is worth pointing out that the backward heat equation has been a hot topic in recent years. In this connection, it is worth citing the group preserving scheme of Liu [18], operator-splitting method of Kirkup and Wadsworth [19], lattice-free finite difference method of Iijima and Onishi [20], global space–time multiquadric method of Li and Mao [21], and discretized Tikhonov regularization by reproducing kernel Hilbert space method of Hon and Takeushi [22]. As mentioned earlier, the method used in this paper is much different from these methods. Our method is an improvement over existing quasi-reversibilty methods in two specific ways: careful use of filtering of high frequency modes and careful selection of space and time steps so that numerical dispersion relation agrees very closely to that of the exact dispersion relation over most participating wave numbers. No application of filtering technique in a clever way as in the technique presented in this paper has been attempted in the past with the backward heat conduction problem. Whereas the regularization by

structural perturbation of the backward equation is known, it has not been used with a purely spatial derivative term as a regularizing term, unlike Xiong [28] who uses a partial time-spatial derivative term.

The paper is laid out as follows. For the sake of completeness, we describe the numerical discretization schemes in Sections 2.1 and 2.2 of Section 2. Section 2.3 details results of numerical computations with these schemes on two examples without any use of the regularization techniques. The purpose is to show the need of regularization techniques which we do in Sections 3 and 4. In Section 3, we show the results of using filters and in Section 4, we show results obtained using structural perturbation, a kind of regularization, of the heat equation. Finally, we conclude in Section 5.

2. Numerical schemes and results

The computational domain Ω is taken to be one-dimensional, in particular $\Omega = [0,1]$. We discretize the interval $[0,1]$ with M subintervals $\Delta x = 1/M$ of equal length with grid points denoted by x_m, $m = 0,\ldots,M$. Integration in time is done in time step of Δt up to time $T = N \times \Delta t$, for some integer N. We denote $t_n = n \times \Delta t$, $n = 0,\ldots,N$. The exact value of the solution at (x_m,t_n) is denoted by $v(x_m,t_n)$ and numerical value by v_m^n. Zero Neumann boundary conditions at both end points of the interval $[0,1]$ are approximated that results in the following third order accurate end point values of v for $t > 0$.

$$v(0,t) = \frac{4v(\Delta x,t) - v(2\Delta x,t)}{3} + O((\Delta x)^3), \tag{4}$$

$$v(L,t) = \frac{4v(1-\Delta x,t) - v(1-2\Delta x,t)}{3} + O((\Delta x)^3). \tag{5}$$

2.1. Euler scheme

In terms of forward and backward finite difference operators D^+ and D^-, the finite difference equation for the backward heat equation is

$$\frac{D_t^+ v_m^n}{\Delta t} = -\nu \frac{D_x^+ D_x^- v_m^n}{\Delta x^2}, \quad \forall m \neq \{1,M\}, \quad \forall n > 2. \tag{6}$$

For numerical construction of solutions, it is useful to choose appropriate values of Δx and Δt so that numerical and exact dispersion relations do not deviate too much from each other over a range of participating wave numbers. Using the ansatz $v_m^n = \rho^n e^{i\xi m}$, (where $\rho = e^{\beta \Delta t}$ and $\xi = k\pi\Delta x$) in the finite difference equation (6) yields the dispersion relation

$$\rho = 1 + 4\nu r \sin^2(k\pi\Delta x/2), \tag{7}$$

where $r = \Delta t/\Delta x^2$. When $\Delta x \to 0$, we have $\rho \sim 1 + (k\pi)^2 \nu \Delta t$ which gives, in the limit $\Delta t \to 0$, $\beta = \ln|\rho|/\Delta t \sim \nu(k\pi)^2$ which is same as the exact growth rate.

2.2. Crank–Nicolson scheme

The backward heat equation in this scheme is discretized as

$$\frac{D_t^+ v_m^n}{\Delta t} = -\frac{\nu}{2\Delta x^2}\left(D_x^+ D_x^- v_m^{n+1} + D_x^+ D_x^- v_m^n\right). \tag{8}$$

For dispersion relation, same ansatz for v_m^n as in the Euler scheme is inserted in the finite difference equation (8). This yields the dispersion relation

$$\rho = \frac{1 + 2\nu r \sin^2\left(\frac{\xi}{2}\right)}{1 - 2\nu r \sin^2\frac{\xi}{2}}, \tag{9}$$

where $r = \Delta t/\Delta x^2$ as before. When $\Delta x \to 0$, we have

$$\rho \sim \frac{1 + \nu(k\pi)^2 \frac{\Delta t}{2}}{1 - \nu(k\pi)^2 \frac{\Delta t}{2}},$$

which gives, in the limit $\Delta t \to 0$, $\beta = \ln|\rho|/\Delta t \sim \nu(k\pi)^2$ which is the same as the exact dispersion relation. For $r > 1/2\nu$, the dispersion relation has a singularity at $k = k_u$ given by

$$k_u = \frac{2}{\pi\Delta x} \arcsin\left(\frac{\Delta x}{\sqrt{2\nu\Delta t}}\right). \tag{10}$$

Fig. 1(a) and (b) compare the exact dispersion relations with the numerical ones for several values of space and time steps respectively for both the Euler and CN schemes. The plots are log–log plots due to the large values of growth rates. Numerical dispersion plot for the CN scheme corresponding to $\Delta x = 10^{-3}$ and $\Delta t = 10^{-4}$ for which $r > 1/2\nu$ clearly shows the location of

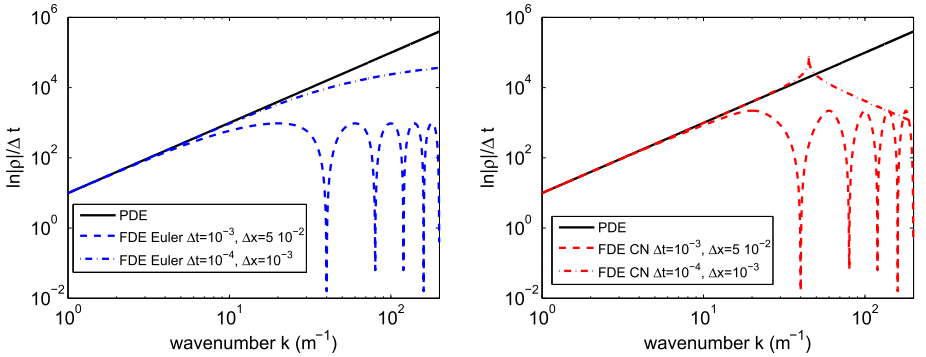

Fig. 1. Comparison in log–log scale of dispersion relations for the PDE and numerical schemes at various values of space and time steps. FDE stands for "Finite Difference Equation". Note the singularity at $k_u = 45.05$ of the Crank–Nicolson FDE for $\Delta t = 10^{-4}$ and $\Delta x = 10^{-3}$.

the singularity at $k_u = 45.05$. Since the singularity and high values of the growth rate are very localized near a very high wave number with rest of the dispersion curves comparing favorably with the exact one, larger time steps may still be able to yield reasonably accurate solutions on the same grid Δx as for the other dispersion curves in the figure. We will test below whether this is indeed true or not. For the other choice of grid values used with CN scheme in the figure, $r < 1/2v$. This figure shows that numerical dispersion curves compare favorably with the exact one up to a higher wave number for the CN scheme than for the Euler scheme. However, they all are almost same for up to a wave number approximately 25 for the CN scheme and 10 for the Euler scheme. For the numerical experiments presented in the next sections, the time step has been fixed at 10^{-4} and the number of space steps $M = 33$. These choices are in agreement with the analysis of the finite difference equation.

2.3. Numerical results

Numerical experiments have been performed on two problems: problem 1 deals with the triangle function and the problem 2 deals with the Heaviside function.

2.3.1. Initial conditions

Example 1 (*Triangle function*). A triangular function on [0,1] is expressed in dimensionless variable by the relation

$$u_0(x) = \begin{cases} 2x & \text{if } x < \frac{1}{2}, \\ 2(1-x) & \text{if } x > \frac{1}{2}. \end{cases} \tag{11}$$

The exact solution at any time t of the forward problem with initial data (11) is given by

$$u(x,t) = a_0 + 2\sum_{k=1}^{\infty} a_k \cos(2k\pi x) e^{-\nu(2k\pi)^2 t}, \tag{12}$$

where

$$a_0 = 1/2, \quad a_k = \frac{(-1)^k - 1}{(k\pi)^2}, \quad k \geqslant 1. \tag{13}$$

It then follows that the exact solution of the backward heat equation with initial data

$$v_0(x) \equiv v(x,0) = a_0 + 2\sum_{k=1}^{\infty} a_k \cos(2k\pi x) e^{-\nu(2k\pi)^2 T_0} \tag{14}$$

is given by

$$v(x,t) = a_0 + 2\sum_{k=1}^{\infty} a_k \cos(2k\pi x) e^{-\nu(2k\pi)^2 (T_0 - t)}, \quad 0 \leqslant t \leqslant T_0. \tag{15}$$

Example 2 (*Heaviside function*). The Heaviside function is given by

$$H(x) = \begin{cases} 0, & \text{if } x < 1/2, \\ 1, & \text{if } x > 1/2. \end{cases} \tag{16}$$

The exact solution of the forward problem with this Heaviside function as initial data is given by

$$u(x,t) = a_0 + 2\sum_{k=1}^{\infty} a_k \cos(k\pi x)\, e^{-\nu k^2 \pi^2 t}, \tag{17}$$

where

$$a_0 = 1/2, \quad a_k = -\frac{1}{k\pi}\sin\left(\frac{k\pi}{2}\right). \tag{18}$$

It then follows that the exact solution of the backward heat equation with initial data

$$v_0(x) \equiv v(x,0) = a_0 + 2\sum_{k=1}^{\infty} a_k \cos(k\pi x)\, e^{-\nu k^2 \pi^2 T_0} \tag{19}$$

is given by

$$v(x,t) = a_0 + 2\sum_{k=1}^{\infty} a_k \cos(k\pi x)\, e^{-\nu k^2 \pi^2 (T_0 - t)}, \quad 0 \leqslant t \leqslant T_0. \tag{20}$$

It is found that fifty modes are more than sufficient to construct reasonably good smooth approximations of the above two singular functions with corners and discontinuities. Therefore, the initial data $v(x,0)$ for the backward heat equation for these two examples has been generated with fifty modes. For each of the examples above, using both the Euler and the Crank–Nicolson schemes we compute numerical solutions $v(x,t)$ from initial data $v_0(x)$ using 14-digit accurate arithmetic.

First of all, we want to emphasize that we solve the backward heat equation in a finite interval. For a solution to exist, following condition on initial data should be satisfied: "amplitude of the Fourier coefficient should decay faster than e^{-k^2} for a mode with wave number k for large k (see also Section 2.2 of [23])". Since we construct the initial data from finite number of modes as explained mode, for both the examples, the above condition is satisfied initially. At later times, this condition is also satisfied because of our use of sharp filter and regularization parameter (see next two sections). Our method thus does not try to recover the exact singular solutions but their smooth approximations. For this purpose, always finite number of modes participate in constructing the solution at any given time, thereby ensuring that the above condition is satisfied. Alternatively, this implies that the initial data we use for these examples satisfy the Picard criterion (see page 39 of [23]) which for the problem of backward heat conduction is $\sum e^{(2k)^2}|f_k| < \infty$ (see Section 1.5 of [23]).

2.3.2. Error growth

In each of the examples above, solution $u(\cdot,T_0)$ for some choice of T_0 is used as the initial data $v(\cdot,0)$ (see (14), (19)) of the backward problem to numerically compute the solution $v(\cdot,t)$ of the backward heat equation for $t \leqslant T_0$. Exact solution $v_e(\cdot,t)$ of the backward heat equation is thus the initial data of the forward problem, i.e., $v_e(\cdot,t) = u(\cdot,T_0 - t)$. Comparison between exact solution $v_e(\cdot,t)$ and numerical solution $v(\cdot,t)$ at time t is done through the normalized L_2 norm of the error defined by

$$e_{L_2}(t) = \frac{\|v(\cdot,t) - v_e(\cdot,t)\|_2}{\|v_e(\cdot,t)\|_2}. \tag{21}$$

Fig. 2(a) shows plots of exact (triangle data (11)) and numerical solutions for Example 1 based on the initial data (14) with $T_0 = 2 \times 10^{-3}$. We see that the solutions are in good agreement except near the end points. Similar numerical results are obtained for Example 2 with initial data (19) and $T_0 = 4.7 \times 10^{-3}$. This is shown in Fig. 2(b) compares the numerical solution at $t = T_0$ with the initial data. These results shown in Fig. 2(a) have been obtained with time step size $\Delta t = 10^{-5}$.

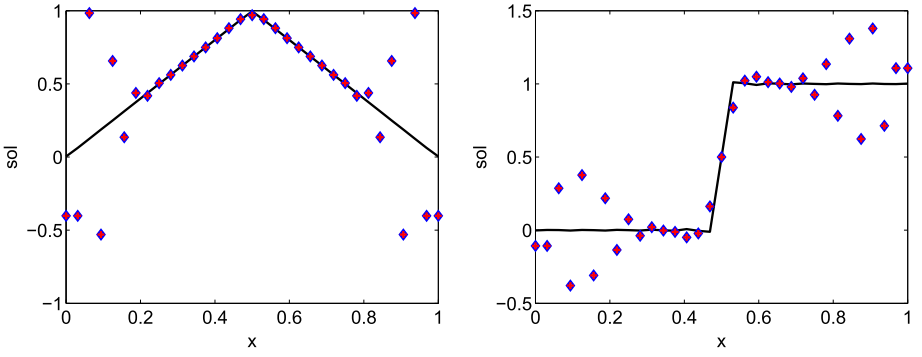

(a) Example 1: $t = T_0 = 2 \times 10^{-3}$. (b) Example 2: $t = T_0 = 4.7 \times 10^{-3}$.

Fig. 2. Comparison of exact (solid line) and numerical solutions (Euler in diamonds and CN in plus, they are on the top of each other) at fixed time for the two examples.

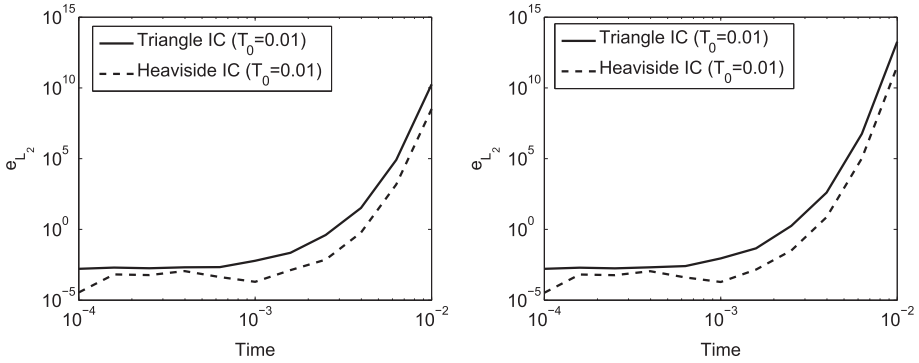

Fig. 3. Log–log plot of L_2 error versus time for two different examples (no noise).

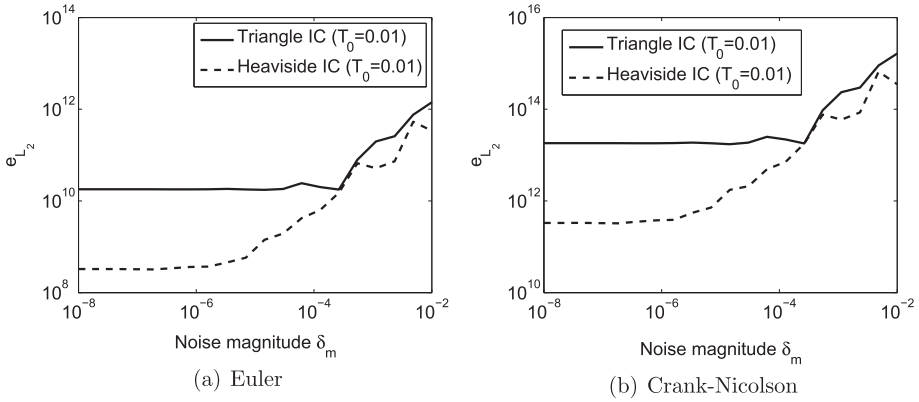

Fig. 4. Log–log plot of L_2 error at $t = 10^{-2}$ versus noise parameter δ_m for two different examples.

For time levels beyond these, i.e. for larger values of T_0 in each of these examples, the accuracy of solutions gradually deteriorates due to growth of participating short waves present in the round-off and the truncation errors. Growth of errors in time is shown in Fig. 3 for both the schemes on two examples when there is no noise. In log–log scale, these plots clearly show a quadratic growth of the error as a function of time. The catastropic growth of error as $t \to T_0$ is expected due to severe illposedness. We show later suitability of the filtering and regularizing techniques in suppressing this growth to some extent and in providing smooth numerical solutions which agree almost everywhere to the non-smooth exact solutions. But first we assess the effect of noise on the error.

2.3.3. Influence of noise

Errors with noisy initial data usually depend on the noise level. Consider the noisy initial data $v^\delta(x,0)$ defined by

$$v^\delta(x,0) = v_0(x) + \delta(x) \times \|v_0(x)\|_\infty, \tag{22}$$

where $v_0(x) = v(x,0)$ (see (14) for Example 1 and (19) for Example 2) and $\delta(x)$ defined by

$$\delta(x) = \delta_m \times \mathrm{rand}(x) \tag{23}$$

is the noise generated using the MatLab function "rand" multiplied by a noise parameter δ_m. Notice that the noise is introduced in such a way that it is proportional to the data $v_0(x)$. For a fixed time $t = 10^{-2}$, Fig. 4 shows the plots of the L_2 error as a function of the noise parameter δ_m for both the Euler and the Crank–Nicolson schemes. For the noisy initial data for Example 1, noise increases the error when the noise parameter becomes larger than 10^{-4}. For Example 2 with noisy initial data, Fig. 4(b) shows that error is more sensitive when the noise parameter exceeds the value 10^{-6}. Below these values, the error remains at a constant level ($O(10^{10})$ for Euler and $O(10^{13})$ for CN) corresponding to the values that can be observed without noise at $t = T_0 = 10^{-2}$ in Fig. 3. Under same numerical conditions and same noise parameter, error with the Crank–Nicolson scheme is three orders of magnitude larger than that with the Euler scheme.

Next two sections discuss a filtering technique and a regularization technique respectively. These have been found suitable to delay the growth of errors. This helps in finding smooth solutions at least for longer time than otherwise possible. The goal below is to show that these numerical solutions are in good agreement with exact non-smooth solutions almost everywhere except near the singularities such as corners and discontinuities for the examples discussed before.

3. Filtering method and results

3.1. Presentation of filtering technique

We have applied five different filters to control the spurious effects on the solution due to catastrophic growth of participating short wave components of the round-off and truncation errors. This results in the filtered spectrum defined by

$$a'_k(k;k_c) = \Phi(k;k_c)a_k(k), \tag{24}$$

where a_k and a'_k denote respectively the unfiltered and filtered Fourier coefficients and k_c is a parameter, called cut-off wave number, on which the filter depends (see below). Since high wavenumber modes are more problematic, all these filters are low-pass filters differing only on their degree of smoothness. All these filters have been discussed in [7]. The simplest of these filters is the sharp filter Φ_s defined by

$$\Phi_s(k) = \begin{cases} 1, & k \leqslant k_c, \\ 0, & k > k_c. \end{cases} \tag{25}$$

This and other filters have been applied to control the error growth but results with the above sharp filter will only be presented as no significant improvement in numerical results was noticed with the other filters. The application of this filter essentially sets amplitudes of all the modes above the cut-off k_c to zero but the filter is applied periodically every p time steps. This application procedure has been used before on other illposed problems (see [16]). It is worth mentioning here that filters can be applied in more sophisticated ways such as filtering only those modes of the solution whose magnitudes are below a pre-determined threshold 10^{-m} slightly above the roundoff error while allowing modes whose values jump above this threshold in one time step to grow (see [5]). But such sophisticated techniques are not necessary if the goal is to obtain a smooth approximations even when the exact solutions may not be C^∞.

3.2. Numerical results

Fig. 5(a) and (b) compare the exact solutions against the numerical solutions. Table 1 recaps the error as a function of the filter parameters: k_c and p. In each case, these parameters have been selected after many runs in order to reach the maximum simulation time under the constraint of constructing the best approximate solutions to the exact ones. These figures show that application of the filter enables computation of solutions which are in agreement with exact ones for times longer than what is otherwise possible without filtering.

Next we show results obtained with noisy initial data (22). Solutions analogous to those shown in Fig. 5(a) and (b) but with these noisy initial data are shown in Fig. 6(a) and (b). Table 2 shows the error norms and values of the different parameters that have been used.

Finally, we test the suitability of the method on a third problem which is constructed as follows. We construct a smooth initial data from superposition of initial data (14) (which is the solution at time T_0 of the forward heat equation with triangle initial data (11)) and an initial data (which is the solution at time T_0 of forward heat equation with Gaussian initial data) taken from [7]. This superposed new initial data for the backward heat equation is shown as black dash dot plot in

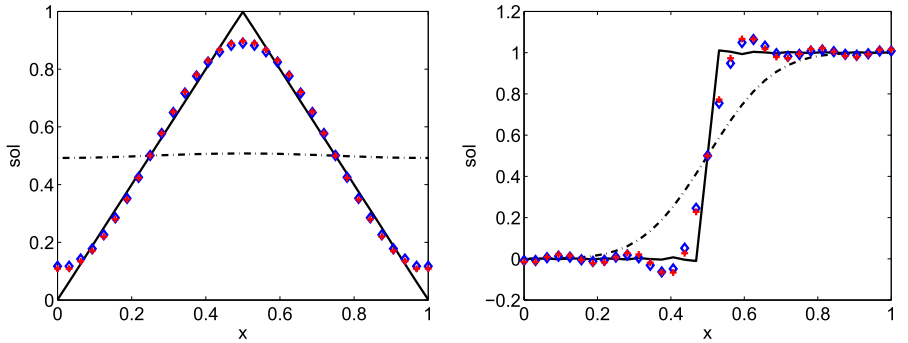

(a) Example 1: $t = T_0 = 0.1$, $k_c = 4$ and $p = 3$. (b) Example 2: $t = T_0 = 0.01$, $k_c = 10$ and $p = 4$.

Fig. 5. Comparison of exact (solid line) and filtered numerical solutions (Euler in diamonds and CN in plus, they may be on the top of each other) for the two examples. Black dash dot line plots the initial condition of the backward problem.

Table 1
Relative error norms using filtering.

IC	Δt	Time	Filter param.	Scheme	e_{L_2}
Example 1	10^{-4}	$t = 0.1$	$k_c = 4$	Euler	6.66×10^{-2}
		$T_0 = 0.1$	$p = 3$	CN	6.41×10^{-2}
Example 2	10^{-4}	$t = 0.01$	$k_c = 10$	Euler	9.91×10^{-2}
		$T_0 = 0.01$	$p = 4$	CN	9.46×10^{-2}

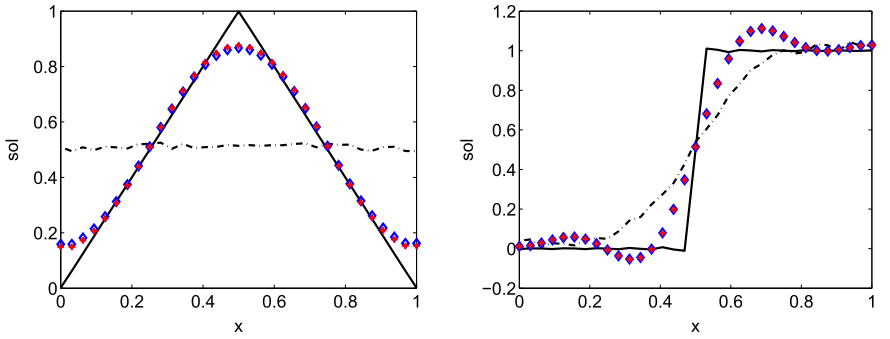

(a) Example 1: $t = T_0 = 0.1$, $k_c = 3$ and $p = 3$. (b) Example 2: $t = T_0 = 0.01$, $k_c = 6$ and $p = 4$.

Fig. 6. Comparison of exact (solid line) and filtered numerical solutions (Euler in diamonds and CN in plus, they may be on the top of each other) for two different examples with noise. Black dash dot line plots the initial condition of the backward problem. Noise parameter is $\delta_m = 5\%$.

Table 2
Relative error norms with the two examples using filtering on noisy initial data.

IC	Δt	Time	Filter param.	Schemes	e_{L_2}
Example 1	10^{-4}	$t = 0.1$	$k_c = 3$	Euler	9.08×10^{-2}
		$T_0 = 0.1$	$p = 3$	CN	8.34×10^{-2}
Example 2	10^{-4}	$t = 0.01$	$k_c = 6$	Euler	1.54×10^{-1}
		$T_0 = 0.01$	$p = 4$	CN	1.54×10^{-1}

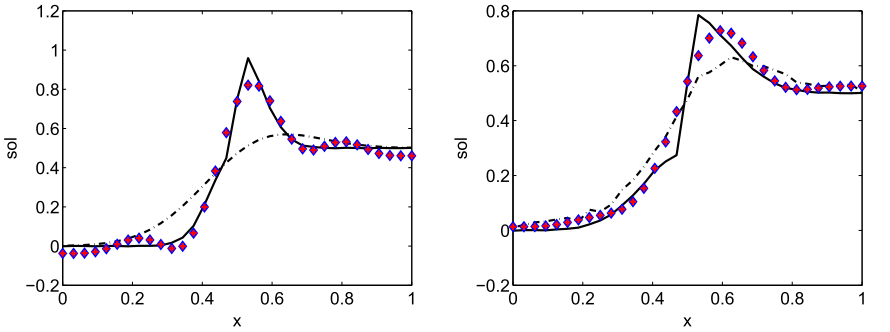

(a) Case without noise: $t = 1 = T_0 = 1$, $k_c = 10$ and $p = 4$.

(b) Case with noise ($\delta_m = 5\%$): $t = T_0 = 0.5$, $k_c = 8$ and $p = 4$.

Fig. 7. Comparison of exact (solid line) and filtered numerical solutions (Euler in diamonds and CN in plus, they may be on the top of each other) for superposition of two different examples: Gaussian ($\nu = 10^{-2}$) with Heaviside initial data (11). Black dash dot line plots the initial condition of the backward problem.

Fig. 7(a). The exact solution of the backward heat equation with this initial data is shown as the solid line in this figure. The numerical solutions as seen in this figure are in reasonably good agreement with the exact solutions except near the corner which is expected since the procedure used is not suitable for producing fine scale features of solutions such as corners. In this case, error $e_{L_2} = 9.77 \times 10^{-2}$. Fig. 7(b) shows analogous results but with noise. Again numerical solutions compare well with the exact solutions. In this case, error $e_{L_2} = 1.08 \times 10^{-1}$.

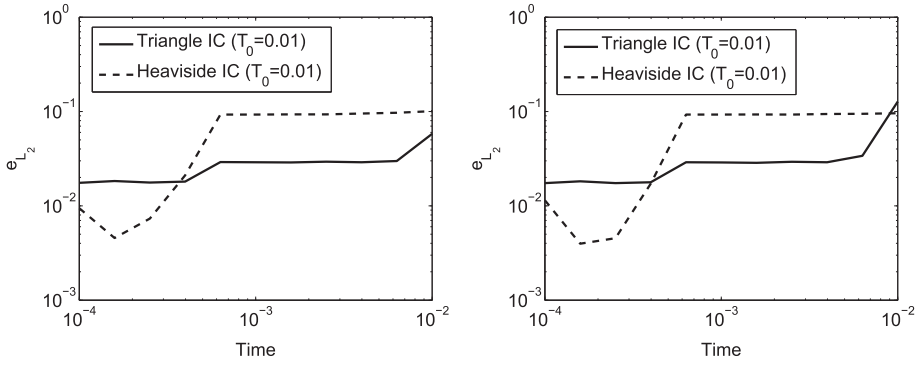

Fig. 8. Log–log plot of L_2 error versus time using filter for two different examples without noise. Filter cut-off is $k_c = 10$ and $p = 4$.

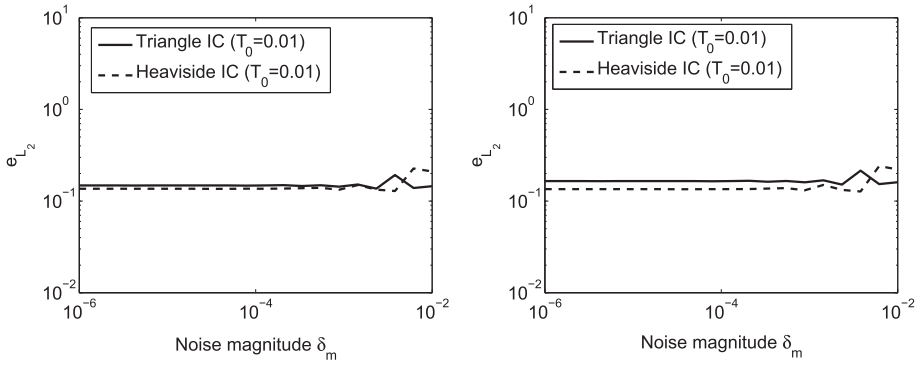

Fig. 9. Log–log plot of L_2 error at $t = 10^{-2}$ versus the noise parameter using filter for two different examples. Filter cut off is $k_c = 6$ and $p = 4$.

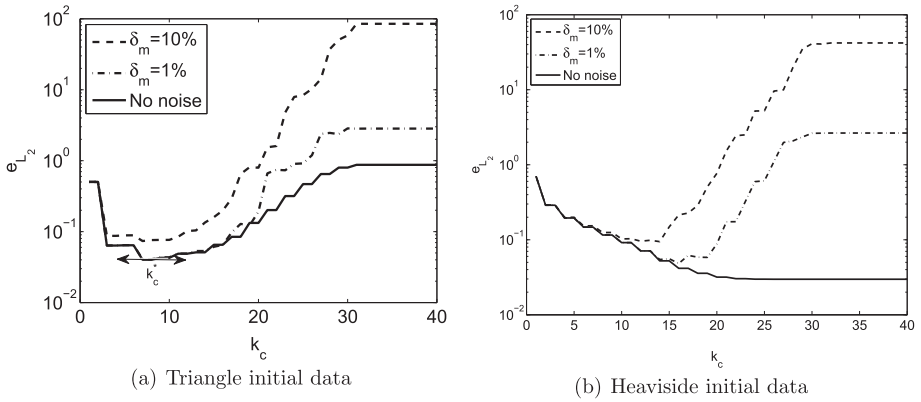

Fig. 10. Semilog plot of L_2 error at $t = 2 \times 10^{-3}$ versus the filter cut off (taken herein as the regularization parameter) with the triangle and Heaviside initial data ($T_0 = 2 \times 10^{-3}$) for three values of the noise parameter δ_m and $p = 1$.

Next we show plots of L_2 error against time for both the numerical schemes in Fig. 8, without any random noise added on the initial data. Then we show results of simulations from initial data with random noise added as per ansatz (22). Fig. 9 shows L_2 error at a fixed time level as a function of the noise parameter δ_m (see (23)). Comparison of Fig. 8 with Fig. 3 shows the effectiveness of the filters in limiting the contamination of the results by spurious growth of the high wave number modes of the round-off and discretization errors. On the other hand, comparison of Fig. 9 with Fig. 4 shows that noise levels $\delta_m < 10^{-4}$ does not affect the L_2 error for the initial condition $v(x,0)$ of Example 2 whereas it does beyond 10^{-3} for the initial

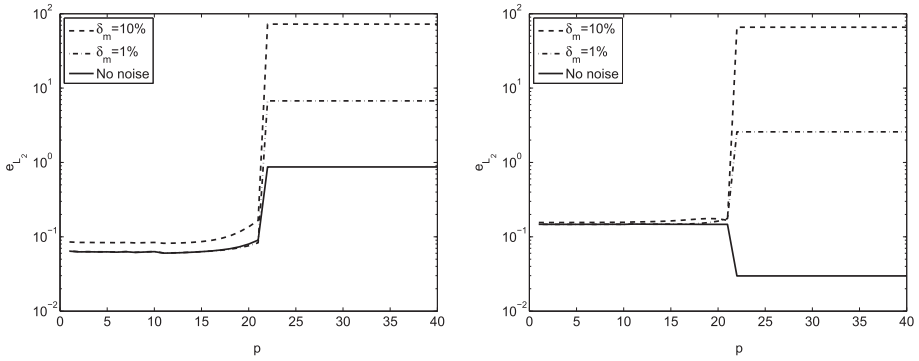

(a) Triangle initial data (b) Heaviside initial data

Fig. 11. Semilog plot of L_2 error at $t = 2 \times 10^{-3}$ versus p (taken herein as the regularization parameter) with the triangle and Heaviside initial data ($T_0 = 2 \times 10^{-3}$) for three values of the noise parameter δ_m and $k_c = 6$.

condition $v(x,0)$ of Example 2. However, as seen in these figures the error in Fig. 9 converges towards much smaller values than those obtained without filter as shown in Fig. 4. The growth of the error is clearly suppressed.

For our purposes below, values of the regularization parameters, k_c (filter cut off) and p (period of application of the filter) for which the L_2 error is least will be called optimal values, denoted by k_c^* and p^* respectively. These optimal values certainly depend on the noise parameter δ_m which is a measure of the signal to noise ratio modulo some constant depending on the examples. A strategy that will allow selection of k_c^* and p^* depending on the noise parameter δ_m is certainly helpful. However, it is not clear how to do this a priori. To get some insight into how to do this even a posteriori, plots of L_2 error are shown against the cut off (Fig. 10) and the period of application of the filter (Fig. 11) for Examples 1 and 2 respectively. The results obtained with the CN scheme only are shown because the results obtained with the Euler scheme show similar plots. The global trend of the Fig. 10 shows a stair function because the filter cut off varies discretely from 1 to 40 and the numerical filter uses a FFT algorithm. Existence of an optimal filter parameter in the range $5 < k_c^* < 10$ is suggested by these plots which is in good agreement with the value chosen for the results presented earlier (see Fig. 5(a) and (b), Fig. 6(a) and (b)). With the filter cut off $k_c^* = 6$ which is in the optimal range of the filter cut off, effect of p on the solution accuracy is shown through several plots in Fig. 11. In this plot, the L_2 error is minimal and grows very slowly for $p < 20$. Beyond this value, there is small window in p around $p = 20$ where the error grows significantly in most (but not all, see Fig. 11) cases. Beyond this value of p (which is between 20 and 22), error hardly grows.

4. Regularization by structural perturbation

4.1. Preliminaries on the technique and schemes

We present this section, even though this section overlaps somewhat with [7], as it is relevant for presenting and understanding the numerical results presented later.

4.1.1. Structural perturbation of the problem

There exists different types of regularization techniques (see [24–26,17,27]). Here we regularize the backward heat equation by adding a fourth order term. The resulting problem is given by

$$\begin{cases} v_t + v v_{xx} + \epsilon v_{xxxx} = 0, & x \in \Omega = [0,1], \quad t \in [0,T], \\ v_x|_{\partial\Omega} = 0, & t \in [0,T], \\ v_{xxx}|_{\partial\Omega} = 0, & t \in [0,T], \\ v(x,0) = \psi(x), & x \in \Omega. \end{cases} \tag{26}$$

The dispersion relation of this Eq. $(26)_1$ is given by:

$$\omega = (\pi k)^2 (\nu - \epsilon(\pi k)^2). \tag{27}$$

The most dangerous wave number k_d with the maximum growth rate $\omega_{\max}$ and the wave number k^* of the neutral mode are given by

$$k_d = \frac{1}{\pi}\sqrt{\frac{\nu}{2\epsilon}}, \quad \omega_{\max} = \frac{\nu^2}{4\epsilon}, \quad k^* = \frac{1}{\pi}\sqrt{\frac{\nu}{\epsilon}}. \tag{28}$$

An appropriate choice of small value for the regularizing parameter ϵ can significantly curtail the spurious growth of short waves. We can see from the above formulas that we can equivalently treat k_d or k^* as regularizing parameter instead of ϵ as

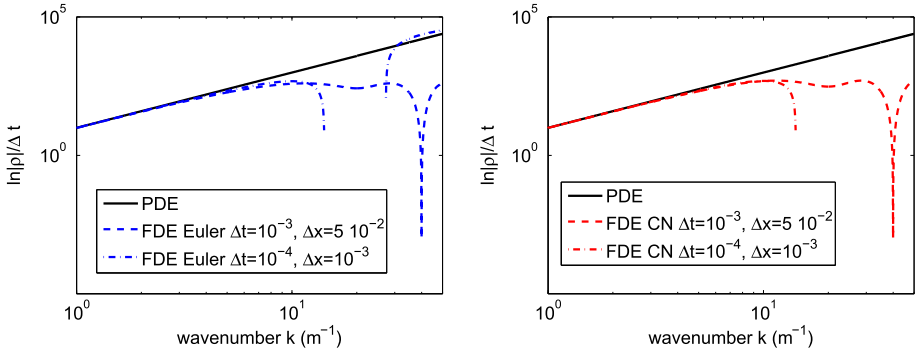

(a) Euler scheme (b) CN scheme

Fig. 12. Comparison in log–log scale of the exact (ω versus k) and numerical ($|\rho|/\Delta t$ versus k) dispersion relations for the regularized problem for several values of space and time steps. For these plots $v = 1$ and $k_d = 10$.

value of ϵ is automatically chosen if we choose either k_d or k^*. Next we discuss the schemes to be used for solving the above regularized problem.

4.1.2. Euler scheme

The finite difference equation for the regularized equation (26) is

$$\frac{D_t^+ v_m^n}{\Delta t} = -v\frac{D_x^+ D_x^- v_m^n}{\Delta x^2} - \epsilon\frac{D_x^+ D_x^- D_x^+ D_x^- v_m^n}{\Delta x^4} \quad \forall\, m \neq \{1, M\}, \quad \forall\, n > 2. \tag{29}$$

For numerical construction of the accurate solutions, it is also necessary to choose appropriate values of Δx and Δt so that numerical and exact dispersion relations do not deviate too much from each other over a range of participating wave numbers. Using the ansatz $v_m^n = \rho^n e^{i\xi m}$, (where $\rho = e^{\beta\Delta t}$ and $\xi = k\pi\Delta x$) in the finite difference equation (29) yields the following dispersion relation for the numerical scheme (29).

$$\rho = 1 + 4r\sin^2\left(\frac{\xi}{2}\right) - 16\mu\sin^4\left(\frac{\xi}{2}\right), \tag{30}$$

where $\mu = \frac{\epsilon\Delta t}{\Delta x^4}$. Fig. 12(a) compares the exact (see Eq. (27)) and the numerical (see Eq. (30)) dispersion relations for several choices of parameter values. This figure shows that the optimal choice for the step sizes are $\Delta x = 10^{-4}$ and $\Delta t = 10^{-3}$ when $v = 1$ and $k_d = 10$. Note that with this set of parameters, the dispersion relation seems to be discontinuous in the range [12,28] of k. In fact, this is due to the representation in log scale of the function that reaches a value close to zero.

4.1.3. Crank–Nicolson scheme

The finite difference equation for the above regularized equation is

$$\frac{D_t^+ v_m^n}{\Delta t} = -\frac{v}{2\Delta x^2}\left(D_x^+ D_x^- v_m^{n+1} + D_x^+ D_x^- v_m^n\right) - \frac{\epsilon}{2\Delta x^4}\left(D_x^+ D_x^- D_x^+ D_x^- v_m^{n+1} + D_x^+ D_x^- D_x^+ D_x^- v_m^n\right). \tag{31}$$

For dispersion relation, same ansatz for v_m^n as in the Euler scheme is inserted in the finite difference equation (31) of the Crank–Nicolson scheme. This yields the following dispersion relation.

$$\rho = \frac{1 + 2r\sin^2\left(\frac{\xi}{2}\right) - 8\mu\sin^4\left(\frac{\xi}{2}\right)}{1 - 2r\sin^2\left(\frac{\xi}{2}\right) + 8\mu\sin^4\left(\frac{\xi}{2}\right)}. \tag{32}$$

Fig. 12(b) compares the exact (see Eq. (27)) and the numerical (see Eq. (30)) dispersion relations for several choices of parameter values. This figure shows that the optimal choice for the step sizes are $\Delta x = 10^{-4}$ and $\Delta t = 10^{-3}$ when $v = 1$ and $k_d = 10$. Note that sometimes the growth factor is undefined in a defined range of wavenumber because some values of ρ are smaller than 1 and plot is done in log scale.

4.1.4. Numerical boundary conditions

This kind of regularization introduces a fourth order term in the equation and a second boundary condition at each boundary (see (26)). The fourth order derivative term is evaluated by finite central differences using five points as follows.

$$v_{xxxx}(x_i, t_j) = \frac{v_{i+2}^j - 4v_{i+1}^j + 6v_i^j - 4v_{i-1}^j + v_{i-2}^j}{\Delta x^4}. \tag{33}$$

Because of this term in the discrete approximation of the regularized equation at the interior grid points, solutions at two points outside the domain, namely v^j_{-1} and v^j_{M+1}, are required. This is done the following way using the second boundary condition (26). The third order derivative term v_{xxx} is approximated to second order accuracy as

$$v_{xxx}|_{x=0} = \frac{-\frac{3}{2}\,v(-\Delta x) + 5\,v(0) - 6\,v(\Delta x) + 3\,v(2\Delta x) - \frac{1}{2}\,v(3\Delta x)}{\Delta x^3} + O(\Delta x^2). \tag{34}$$

Using the boundary condition $v_{xxx} = 0$ and the third order accurate approximation (4) in the above formula, we obtain third order accurate formulae:

$$v(-\Delta x) \simeq \frac{4v(\Delta x) + 8v(2\Delta x) - 3v(3\Delta x)}{9} \tag{35}$$

and similarly at $x = L$ (using Eq. (5)):

$$v(L + \Delta x) \simeq \frac{4v(L - \Delta x) + 8v(L - 2\Delta x) - 3v(L - 3\Delta x)}{9}. \tag{36}$$

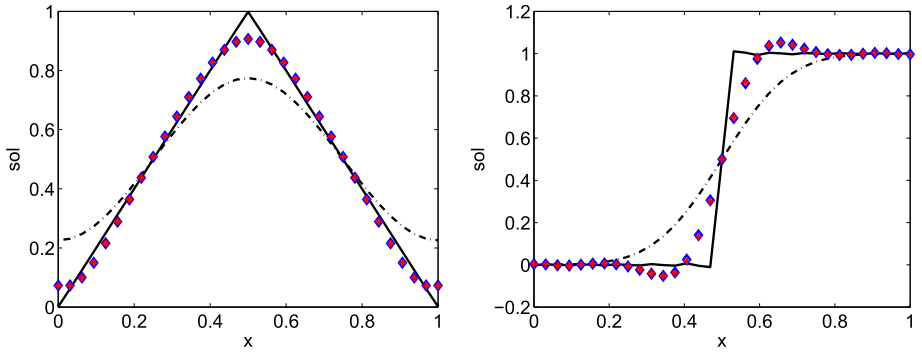

(a) Example 1: $t = T_0 = 0.01$, $k_d = 7$. (b) Example 2: $t = T_0 = 0.01$, $k_d = 10$.

Fig. 13. Comparison of exact (solid line) and numerical solutions (Euler in diamonds and CN in plus, they may be on the top of each other) for the two examples with regularization. Black dash dot line plots the initial condition of the backward problem.

Table 3
Relative error norms with regularization.

IC	Δt	Time	k_d	Schemes	e_{L_2}
Example 1	10^{-4}	$t = 0.01$	$k_d = 7$	Euler	4.54×10^{-2}
		$T_0 = 0.01$		CN	4.53×10^{-2}
Example 2	10^{-4}	$t = 0.01$	$k_d = 10$	Euler	1.35×10^{-1}
		$T_0 = 0.01$		CN	1.34×10^{-1}

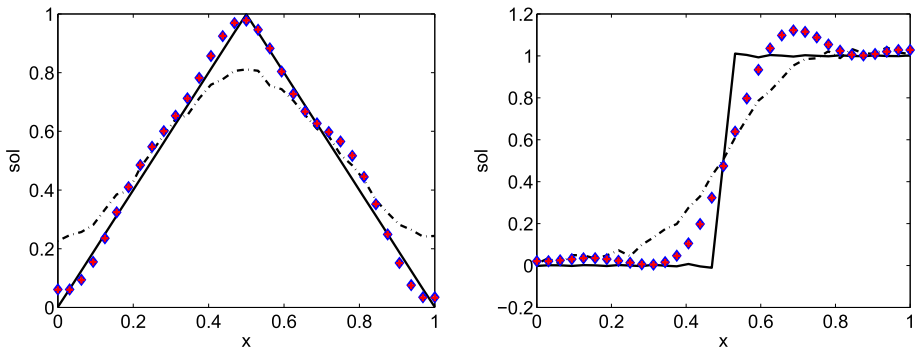

(a) Example 1: $t = T_0 = 0.01$, $k_d = 6$. (b) Example 2: $t = T_0 = 0.01$, $k_d = 6$.

Fig. 14. Comparison of exact (solid line) and numerical solutions (Euler in diamonds and CN in plus, they may be on the top of each other) for the two examples with regularization. Black dash dot line plots the initial condition of the backward problem. Noise parameter is $\delta_m = 5\%$.

Table 4
Relative error norms with regularization on noisy initial conditions.

IC	Δt	Time	k_d	Schemes	e_{L_2}
Example 1	10^{-4}	$t = 0.01$	$k_d = 6$	Euler	6.40×10^{-2}
		$T_0 = 0.01$		CN	6.47×10^{-2}
Example 2	10^{-4}	$t = 0.01$	$k_d = 6$	Euler	1.60×10^{-1}
		$T_0 = 0.01$		CN	1.60×10^{-1}

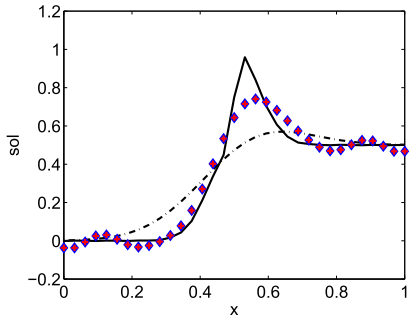

(a) Case without noise: $t = T_0 = 1$, $k_d = 10$.

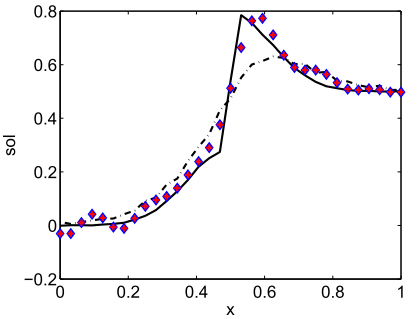

(b) Case with noise ($\delta_m = 5\%$): $t = T_0 = 0.5$, $k_d = 10$.

Fig. 15. Comparison of exact (solid line) and numerical solutions (Euler in diamonds and CN in plus, they may be on the top of each other) using regularization for superposition of two different examples: Gaussian ($\nu = 10^{-2}$) with Heaviside initial data (11). Black dash dot line plots the initial condition of the backward problem.

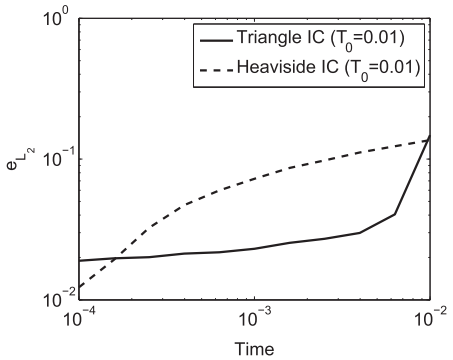

(a) Euler

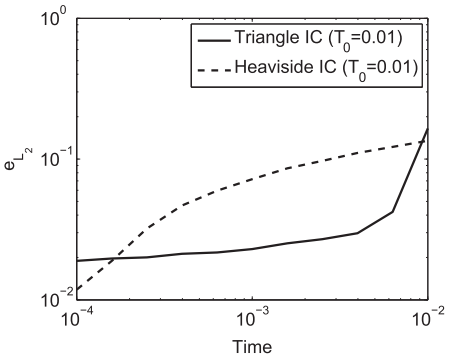

(b) Crank-Nicolson

Fig. 16. Log–log plot of L_2 error versus time for the regularized problem for two examples without noise. Regularization parameter is given by $k_d = 10$.

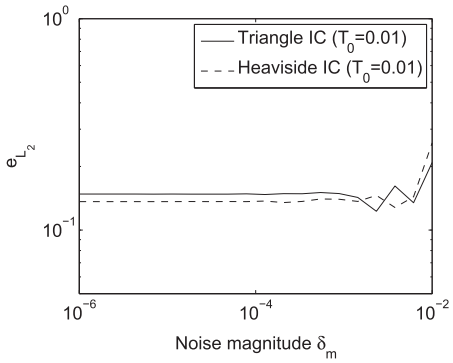

(a) Euler

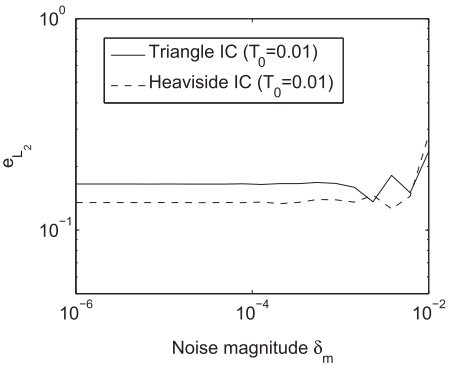

(b) Crank-Nicolson

Fig. 17. Log–log plot of L_2 error at $t = 0.01$ versus the noise parameter δ_m for the regularized problem for two examples. Regularization parameter is given by $k_d = 10$.

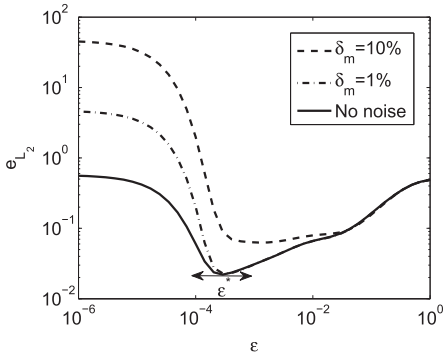

(a) Triangle initial data

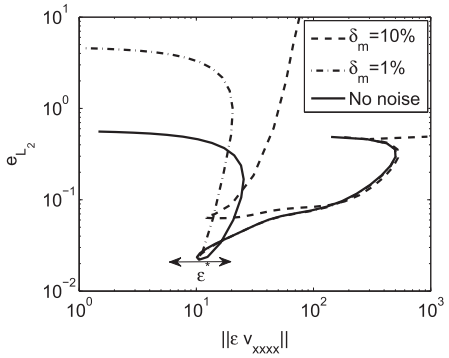

(b) Triangle initial data

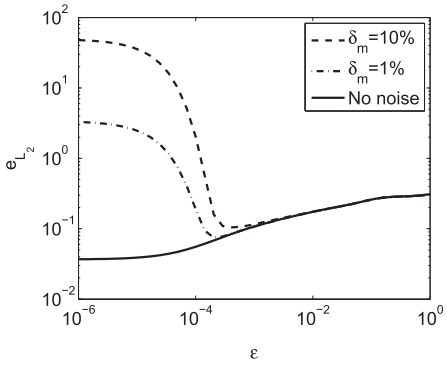

(c) Heaviside initial data

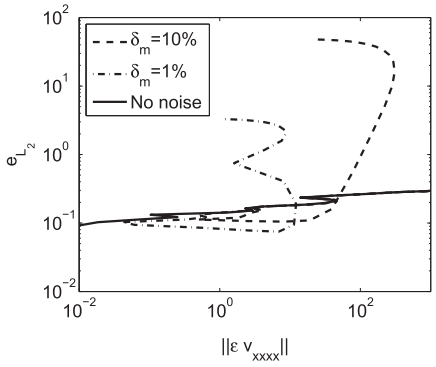

(d) Heaviside initial data

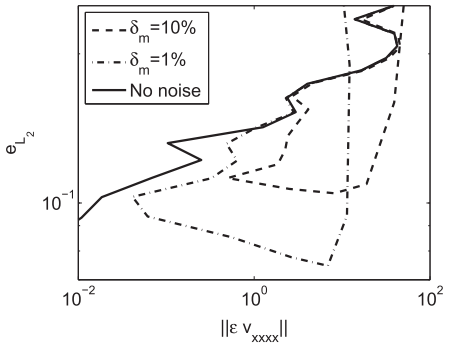

(e) Heaviside initial data (zoom of 18(d))

Fig. 18. Log–log plot of L_2 error at $t = 2 \times 10^{-3}$ versus the regularization parameter ϵ with the triangle and Heaviside initial data ($T_0 = 2 \times 10^{-3}$) for three values of the noise parameter δ_m.

4.2. Numerical results

Fig. 13(a) and (b) compare the numerical solutions of the regularized problem with the exact solutions of the backward heat equation. The normalized L_2 error norms are shown in the Table 3. The parameters for which we obtain the best results for each of these schemes are mentioned in the caption of the figures and are also shown in Table 3. These numerical results confirm that under a given tolerance of error, the simulation time can be increased significantly using regularization.

Finally, we present numerical results for regularized backward problem subject to initial conditions (22) with noise (23). Plots are shown in Fig. 14(a) and (b). Table 4 recaps the error norms. We have also done numerical experiments with the third example discussed earlier where the initial data is constructed from superposition of initial data (14) (which is the solution at time T_0 of the forward heat equation with triangle initial data (11)) and an initial data (which is the solution at time T_0 of forward heat equation with Gaussian initial data) taken from [7]. These initial data with and without noise are same as the ones (dot-dash curves) shown in Fig. 7(a) and (b). In Fig. 15(a) and (b), these initial data and corresponding

Table 5
Values of time and noise parameter after which the solution error grows catastrophically.

Regularization	IC	t^*	δ_m^*
No reg.	Example 1	6×10^{-3}	10^{-4}
	Example 2	10^{-3}	10^{-6}
Filtering	Example 1	4×10^{-4}	3×10^{-3}
	Example 2	?	?
Struct. pert.	Example 1	8×10^{-3}	8×10^{-3}
	Example 2	?	?

solutions for the regularized case are shown and compared with exact solutions (solid lines). In these cases, the errors are $e_{L_2} = 1.42 \times 10^{-1}$ without noise and $e_{L_2} = 8.76 \times 10^{-2}$ with noise.

As before, we present in Fig. 16 the error growth as a function of time for the regularized problem. For these simulations, no random noise has been added on the initial data. The sensitivity of the solutions to noise has also been found to be interesting which is shown through the plots of L_2 error versus noise parameter δ_m in Fig. 17. Comparing Fig. 16 with Figs. 3 and 17 with Fig. 4 respectively, it is observed that regularization suppresses the growth of the error with or without noise. Moreover, its effect is fully comparable to that of the filter (see Figs. 8 and 9).

For our purposes below, value of the regularization parameter ϵ for which the L_2 error is least will be called optimal value, denoted by ϵ^*, of the parameter ϵ. The choice of the optimal value ϵ^* certainly depends on the noise parameter δ_m which is a measure of the signal to noise ratio modulo some constant depending on the examples. A strategy that will allow selection of ϵ^* which depends on the noise parameter δ_m is certainly helpful. However, it is not clear how to do this a priori. To get some insight into how to do this even a posteriori, plots of L_2 error is shown against the regularization parameter ϵ in Fig. 18(a) and Fig. 18(c) for Examples 1 and 2 respectively. Plots of L_2 error is also shown against the residual norm ($\|\epsilon \times v_{xxxx}\|_2$) in Fig. 18(b) and Fig. 18(d) for Examples 1 and 2 respectively. Here again, only the results obtained with CN scheme are presented because of the similarity with the plots for Euler scheme. The plots in Fig. 18(a) and (c) resemble *U*-curves and those in Fig. 18(b) and (d) resemble distorted *L*-curves. Closure scrutiny of the plots Fig. 18(d) in the blow-up Fig. 18(e) shows that for Example 2, the error versus residual plot for no noise case is more of a stair case type, unlike most of the other plots. It is worth mentioning here that computations of L_2 errors and the residual norms were computed for decreasing values of the regularization parameter ϵ and then these plots were done. Therefore, it should be understood that the parameter ϵ decreases as any of the so called distorted *L*-curves in Fig. 18(b) and (d) are traced from right to left. We see from the *U*-curves in Fig. 18(a) and (c) that both, the minimal value of L_2 error (corresponding to ϵ^*) and the optimal value ϵ^* decrease monotonically with decreasing values of the noise parameter δ_m. Notice that the effect of ϵ decreasing away from the optimal value ϵ^* has much more dramatic effect on the L_2 error than on the residual, with both $L-2$ error and residual increasing. In the presence of noise, L_2 error increases rapidly with very little change in the residual (the *L*-part of the *L*-curves). Therefore, either of the curves can be used for choosing the optimal value ϵ^*.

It is worth noting that the *U*-curve for Example 2 with no noise in the initial data does not seem to have a minimum. Actually, this is due to the combination of a small simulation time and the absence of noise that does not lead to any divergence of the computation. Second, for this case L_2 error versus residual plot is really not monotonic. This is made clear in the Fig. 18(e).

For the case of Example 1, we find by closure scrutiny of the data corresponding to plots of Fig. 18(a) that optimal values of the regularization parameter are in the range $2.9 \times 10^{-4} < \epsilon^* < 1.2 \times 10^{-3}$ for the noise level δ_m in the range 0–10%. Using relation (28), this corresponds to the wave number range $6 < k_d < 14$, in good agreement with the values we have used for Fig. 13(a) and Fig. 14(a).

In general, smaller the magnitude of the noise, smaller the optimal value of the regularization parameter ϵ^*. The value of ϵ^* seems to remain constant when the noise parameter δ_m reaches a value less than 0.01 (figure is not shown here). Indeed, for such a value of $\delta_m < 0.01$ and such time level, the error is only slightly affected by the noise in agreement with the observation made in Fig. 4. As seen in the *U*-curves, for optimal choice ϵ^* of the regularizing parameter with noise level $\delta_m < 0.01$ in the initial data, the regularized solution approximates the original one having an L_2 error of the order of $O(10^{-1})$. In concluding this section, we want to emphasize that the discussion here on *U*- and *L*-curves are based on plots made from data obtained at a specific time level. More research is needed (which will be a topic of research in the future) to determine, even a posteriori, an optimal value of the regularizing parameter based on time of simulation.

5. Discussions and conclusions

Before finally summarizing our conclusions, it is appropriate to make comparisons of our numerical results on these two examples with existing works if any. In the case of Example 1, numerical results of Muniz et al. [25] can be compared with ours. Muniz et al. [25] uses "Entropy- and Tikhonov-based regularization techniques" to solve the backward heat equation. In Muniz et al. [25], initial data for the backward problem $v(x,0)$ is obtained from the exact solution at some time T_0 of the forward problem using the initial data $u(x,0)$ given by (11). Noisy data is created there in the same way as we have done here except that the random variable they used is based on the normal distribution as opposed to the one used here which is based on uniform distribution. At the same simulation time $t = 0.01$, they obtain error estimates in the range of

$[10^{-2}, 10^{-1}]$, exactly the same range we obtained for our results with noise. To the best of our knowledge to-date, numerical results on recovering Heaviside function with the backward heat equation (from late time solution of the forward heat equation with Heaviside function as initial data) are not available in the literature. Therefore, no comparison of our results for this example (Example 2) is provided here except with the exact solution.

In both the (filtering and structural perturbation) methods, associated partial differential equations are integrated on a finite difference grid. Time integration is performed by two schemes, Euler and Crank–Nicholson (CN), instead of only Euler scheme because of following two primary reasons: (i) Euler scheme has time step restriction for stability whereas CN scheme does not; (ii) CN scheme's numerical dispersion relation has a singularity meaning the numerical growth rate of a certain wave becomes unbounded (see Fig. 1(b) in [7]). Therefore, it is not only a curiosity and a challenge to make the CN scheme work but also compare its performance with the Euler scheme. Thus, even though for the purpose of solving the inverse problem Euler scheme will suffice, using both schemes allows us to understand the CN scheme for this problem as well as allows a comparison of these two schemes.

It is worth commenting in conclusion on the comparative analysis of the inverse solutions from the filtering and structural perturbation methods. Such an analysis of L_2 errors from Tables 1–4 for eight cases tested show the following. Crank–Nicholson scheme gives best results in 5 occurrences, particularly in every case where initial conditions are not contaminated with noise (Tables 1–3). Euler scheme is the better numerical scheme with regularization technique using triangle initial data (Example 1, Table 4) without noise, whereas both the numerical schemes give similar results with Example 2 with noise (Tables 2 and 4). These results were obtained by optimizing the regularization parameters which may be different in each case. In this situation, CN appears to be a better numerical scheme. On the other hand, when comparing the error maximum in Figs. 3, 4, 8, 9 and 16, 17, L_2 error in the CN scheme reaches higher value than those in the Euler scheme, because the regularization parameters cannot be optimal for both schemes at the same time. From our computational experience with these cases and many others not presented here, we can say that any of these methods can be used so long as the right set of regularization parameters are chosen which, as these examples show, is partly science and art at this stage because these cannot set a priori. However, no significant difference in the results using these different methods could be observed if computations were done with the optimal values of the regularization parameters which are difficult to set a priori. The critical values of time and noise parameter δ_m in these two methods can be different, problem specific and parameter dependent. This issue is addressed next.

Since the ill-posedness become more severe as time interval t and noise level δ_m increase, it is useful to show the critical point of t and δ_m after which the solution error grows catastrophically for various cases listed in the Table 5. Table 5 tabulates the values of the time and noise parameters that cause a catastrophic growth of the solution errors with or without regularization. Simulations at various time levels corresponding to the six cases in the table have been shown earlier in Figs. 3, 4, 8, 9, 16 and 17 respectively. This table shows, in another way, the effect of regularization methods on the error growth: values of these critical points are delayed to larger values due to regularization, thus extending the range of quasi-reversibility of the problems. Comparing the range of the L2 error, no catastrophic growth is observed when using regularization with Example 2 since the plots for this case (dotted lines in Figs. 8 and 16) have concave shapes and the use of catastrophic growth is not appropriate here. Without regularization (Fig. 3), the critical time is smaller than in other cases and the error grows more rapidly and reaches values much larger (Figs. 8 and 16) early.

In summary, two stable ways of computing solutions of the backward heat equation, namely filtering (direct filtering of short waves) and regularization techniques (structural perturbation of the heat equation), have been used in this paper in conjunction with Euler and Crank–Nicolson methods. The goal here has been to test the suitability of these for producing approximate solutions to exact non-smooth solution from smooth initial data. We have shown results on three examples in which final data either has a corner or a jump discontinuity. The methods are found suitable for computing solutions in a stable manner for times longer than otherwise possible. The methods can recover solutions which are in good agreement with the exact singular solutions almost everywhere except in a small neighborhood of the singularities where the numerical solutions are solutions for times longer than otherwise possible. It will be interesting to investigate these issues in higher dimension, specially in two- and three-dimension, using similar methods. In principle, the methods developed here in one-dimension can be extended to higher dimension and should be straight-forward. This is a topic of future research.

Acknowledgments

We sincerely thank the reviewers for their constructive suggestions which have helped us improve the paper. The research of Fabien Ternat and Oscar Orellana has been partially supported by an SCAT grant and that of Prabir Daripa has been partially supported by Grant # NPRP 08-777-1-141 from the Qatar National Research Fund (a member of The Qatar Foundation). Fabien Ternat is particularly grateful to the Mathematics Department of Texas A&M University for providing resources such as office space and computer during a short visit in the month of July 2010 which has made possible the completion of this article. The statements made herein are solely responsibility of the authors.

References

[1] G. Baker, R.E. Caflisch, M. Seigel, Singularity formation during Rayleigh–Taylor instability, J. Fluid Mech. 252 (1993) 51–78.
[2] R. Caflisch, O. Orellana, Singular solutions and illposedness for the evolution of vortex sheets, SIAM J. Math. Anal. 20 (1989) 293–307.

[3] D.D. Joseph, J.C. Saut, Short-wave instability and illposed initial value problems, Theor. Comput. Fluid Dyn. 1 (1990) 191–227.
[4] D.W. Moore, The spontaneous appearance of a singularity in the shape of an evolving vortex sheet, Proc. Roy. Soc. Lond. A 365 (1979) 105–119.
[5] R. Krasny, A study of singularity formation in a vortex sheet by the point-vortex approximation, J. Fluid Mech. 167 (1986) 65–93.
[6] M.J. Shelley, A study of singularity formation in vortex sheet motion by a spectrally accurate vortex method, J. Fluid Mech. 244 (1992) 493–526.
[7] F. Ternat, O. Orellana, P. Daripa, Two stable methods with numerical experiments for solving the backward heat equation, Appl. Numer. Math. 61 (2) (2011) 266–284.
[8] J. Nash, Continuity of solutions of parabolic and elliptic equations, Amer. J. Math. 80 (1958) 931–954.
[9] F. John, Numerical solution of the equation of heat conduction for preceding times, Ann. Mat. Pura. Appl. se. IV 40 (1955) 129–142.
[10] W. Miranker, A well posed problem for the backward heat equation, Proc. Amer. Math. Soc. 12 (1961) 243–247.
[11] K. Höllig, Existence of infinitely many solutions for a forward backward heat equation, Trans. Amer. Math. Soc. 279 (1983) 299–316.
[12] P. Daripa, W. Hua, A numerical study of an ill-posed Boussinesq equation arising in water waves and nonlinear lattices: Filtering and regularization techniques, Appl. Math. Comput. 101 (1999) 159–207.
[13] J.J. Douglas, T.M. Gallie, An approximate solution of an improper boundary value problem, Duke Math. J. 26 (1959) 339–347.
[14] C. Pucci, sui problemidi cauchynon "ben posti", Atti Accad. Naz. Lincei. Rend. Cl. Sci. Fis. Mat. Nat. 18 (1955) 473–477.
[15] I. Seidman, Optimal filtering for the backward heat equation, SIAM, J. Numer. Anal. 33 (1996) 162–170.
[16] P. Daripa, Some useful filtering techniques for illposed problems, J. Comput. Appl. Math. 100 (1998) 161–171.
[17] C.-L. Fu, X.-T. Xiong, Z. Qian, Fourier regularization for a backward heat equation, J. Math. Anal. Appl. 331 (2007) 472–480.
[18] C.S. Liu, Group preserving scheme for backward heat conduction problems, Int. J. Heat Mass Transfer 47 (2004) 2567–2576.
[19] S. Kirkup, M. Wadsworth, Solution of inverse diffusion problems by operator-splitting methods, Appl. Math. Modell. 26 (2002) 1003–1018.
[20] K. Iijima, K. Onishi, Lattice-free finite difference method for numerical solution of inverse heat conduction problem, Inverse Problems Sci. Eng. 15 (2007) 93–106.
[21] Z. Li, X.Z. Mao, Global space-time multiquadratic method for inverse heat conduction problems, Int. J. Numer. Methods Eng. 85 (2011) 355–379.
[22] Y.C. Hon, T. Takeushi, Discretized Tikhonov regularization by reproducing kernel Hilbert space for backward heat conduction problem, Adv. Comput. Math. 34 (2011) 167–183.
[23] H. Engl, M. Hanke, A. Neubauer, Regularization of Inverse Problems, Kluwer Academic Publishers, 2000.
[24] K.A. Ames, L.E. Payne, Asymptotic behavior for two regularizations of the cauchy problem for the backward heat equation, Math. Models Methods Appl. Sci. 8 (1998) 187–202.
[25] W.B. Muniz, F.M. Ramos, H.F.D. Velho, Entropy- and Tikhonov-based regularization techniques applied to the backwards heat equation, Comput. Math. Appl. 40 (2000) 1071–1084.
[26] N.S. Mera, L. Elliott, D.B. Ingham, An inversion method with decreasing regularization for the backward heat conduction problem, Numer. Heat Transfer, Part B 42 (2002) 215–230.
[27] G. Teschke, M. Zhariy, M.J. Soares, A regularization of nonlinear diffusion equations in a multiresolution framework, Math. Methods Appl. Sci. 31 (2008) 575–587.
[28] X.-T. Xiong, -L. Fu, A. Qian, Two numerical methods for solving a backward heat conduction problem, Appl. Math. Comput. 179 (2006) 370–377.